Int. J. Anal. Appl. (2026), 24:299

International Journal of Analysis and Applications

Analysis and Numerical Approximation of a Rainfall-Derivative Pricing Equation

Tareq Saeed[1,*], **Javed Hussain**[2], **Ashraf M. Zenkour**[3], **Abdullah O. Alshammari**[1]

[1]*Financial Mathematics and Actuarial Science Research Group, King Abdulaziz University, P.O. Box 80203, Jeddah 21589, Saudi Arabia*

[2]*Department of Mathematics, Sukkur IBA University, Pakistan*

[3]*Department of Mathematics, Faculty of Science, King Abdulaziz University, P.O. Box 80203, Jeddah 21589, Saudi Arabia*

Corresponding author: tsalmalki@kau.edu.sa

Abstract. Rainfall derivatives are useful when precipitation risk affects agricultural production, water management, or other climate-sensitive activities, but their pricing differs from the pricing of traded financial assets. We study a rainfall-index contract whose state variables are the current rainfall intensity and an accumulated deficit index. The rainfall intensity follows a seasonally forced Ornstein–Uhlenbeck model, and the index records the time spent below a reference rainfall level. After choosing an equivalent pricing measure through a constant market price of rainfall risk, we obtain a backward valuation equation with diffusion in the rainfall variable and one-sided transport in the index variable. The paper analyses this parabolic–transport problem and then uses the analysis to guide computation. We prove an energy estimate, continuous dependence on the data, well-posedness, comparison, positivity, and monotonicity in the cumulative index. We also construct an explicit finite-difference benchmark with an upwind treatment of the transported variable and compare it with a residual-based parametric approximation. The error estimate relates the approximation error to the PDE residual and the boundary and initial mismatches. The calibrated examples use seven Saudi rainfall regimes. Across these cases the residual-based approximation remains close to the finite-difference benchmark, with relative L^2-errors below 9×10^{-2}. The sensitivity results are not uniform across regions. Arid interior cities show weak volatility exposure, Makkah and Medina are more responsive to mean reversion and volatility, and Abha has negative sensitivities under the put payoff convention. These differences support regime-specific calibration rather than a single national rainfall parameter set.

1. Introduction

Weather derivatives provide a way to transfer financial risk generated by ordinary but economically damaging deviations in weather. They are used in agriculture, water management, energy

Received: Jun. 19, 2026.

2020 *Mathematics Subject Classification.* 35K15, 35K20, 35Q91, 60H10, 65M06, 65M12, 91G20, 91G60.

Key words and phrases. rainfall derivatives; weather derivatives; Ornstein–Uhlenbeck process; parabolic–transport equation; energy estimate; finite-difference method; residual-based approximation; climate-risk valuation.

https://doi.org/10.28924/2291-8639-24-2026-299

ISSN: 2291-8639

production, transportation, and tourism, where revenue can depend directly on temperature, rainfall, snowfall, or wind conditions [26, 27]. Rainfall-linked contracts are especially relevant in regions where water availability constrains production and planning. A long dry period may reduce agricultural output, affect reservoir operation, or increase the cost of municipal water supply. Such losses are often gradual rather than catastrophic. This makes index-based contracts a natural tool: the payoff is tied to an observed rainfall index, not to a claims-adjustment process.

Pricing such contracts is not a direct extension of the Black–Scholes theory. Rainfall is not a traded asset, so replication does not identify a unique equivalent martingale measure in the way it does for liquid financial securities [22]. A pricing model must therefore specify both the rainfall dynamics and the risk adjustment used for valuation. We work with a seasonally forced Ornstein–Uhlenbeck intensity process and an accumulated deficit index. If x denotes current rainfall intensity, y the accumulated index, and τ backward time, the value function has the form

$$V = V(x, y, \tau).$$

The resulting equation is

$$V_\tau = \gamma(x, \tau) V_x + f(x) V_y + \frac{\sigma^2}{2} V_{xx} - rV. \tag{1.1}$$

Only the rainfall-intensity variable is diffusive. The index variable is transported. This asymmetric structure is the main technical feature of the paper: it determines the boundary conditions, the upwind direction in the finite-difference scheme, and the form of the residual loss used in the parametric approximation.

Several approaches to weather-derivative pricing already exist. Benth and Šaltytė-Benth [27] give a broad modelling framework for weather-linked markets, while Zeng [26] discusses the early role of weather derivatives in risk management. For precipitation contracts, Carmona and Diko [28] developed pricing methods for rainfall-linked products, and Harris [17], Hamisultane [18], and Broni-Mensah [19] studied PDE-based methods in incomplete-market settings. In the more recent PDE literature, Li [14] derived valuation equations for Ornstein–Uhlenbeck weather models and later introduced one-sided Crank–Nicolson schemes adapted to directional transport [20]. Tang, Yu, and Guo [15] treated mean-reverting jump–diffusion models by a semi-Lagrangian method, and Hess [29] considered multi-factor Ornstein–Uhlenbeck jump dynamics for precipitation derivatives. Nhangumbé and Sousa [16] gave a numerical treatment of a rainfall weather-derivative pricing model and showed how strongly the computation depends on the correct treatment of the index direction.

A separate line of work uses neural networks to approximate solutions of PDEs. Physics-informed neural networks were introduced in [1] as a residual-minimisation approach for forward and inverse problems, and have since been extended to Bayesian and noisy-data settings [2, 6, 8]. In finance, related methods have been used for Black–Scholes-type equations, American options, counterparty credit risk, and stochastic-volatility valuation problems [4, 5, 9–11, 13, 25]. Bansal, Boro, and Natesan [21] applied a physics-informed network to a weather-derivative pricing model.

These works show that residual-based methods can be effective, but for rainfall-index contracts the transport structure still has to be built into the formulation. A small residual is meaningful only when the residual, boundary terms, and index direction correspond to the actual pricing problem.

Our purpose is to join these two strands. Starting from a seasonal mean-reverting rainfall model, we derive the parabolic–transport equation for a cumulative-index contract and prove the stability properties needed for numerical approximation. The energy estimate gives continuous dependence on data and leads to comparison, positivity, and monotonicity in the index variable. We then construct a finite-difference benchmark with the correct upwind treatment in y, and we compare it with a residual-based approximation whose error is controlled by the PDE residual and the boundary and initial mismatches. The empirical part calibrates the model across seven Saudi rainfall regimes. The regional comparison is important because the same payoff reacts differently in arid, transitional, coastal, and high-rainfall settings; in particular, the high-rainfall southwest behaves differently under the put payoff convention.

The paper is organised as follows. Section 2 derives the rainfall dynamics, cumulative index, pricing measure, and valuation equation. Section 3 proves the analytical properties of the pricing problem. Section 4 develops the finite-difference and residual-based approximations. Section 5 gives the calibration procedure and contract parameters. Sections 6–8 report the numerical comparison, regional case studies, and sensitivity analysis. Section 9 concludes with limitations and extensions.

2. Rainfall Dynamics and Derivative Pricing Model

The pricing model has two state variables. The first is the instantaneous rainfall intensity, which carries the random fluctuations. The second is a cumulative rainfall-deficit index, which determines the contract payoff. This separation leads to the mixed structure of the valuation equation: diffusion acts in the rainfall variable, while the cumulative index enters through transport.

Let

$$(\mathcal{S}, \mathcal{F}, \{\mathcal{F}_t\}_{0\le t\le T}, \mathbb{P})$$

be a filtered probability space satisfying the usual conditions and supporting a one-dimensional Brownian motion $W = \{W_t\}_{0\le t\le T}$. The measure $\mathbb{P}$ denotes the physical measure. Calendar time is denoted by t, the maturity is $T > 0$, and backward time is

$$\tau = T - t.$$

Thus $\tau = 0$ corresponds to maturity and $\tau = T$ to the valuation date.

The pricing equation is solved on the truncated cylinder

$$D = [x_{\min}, x_{\max}] \times [0, y_{\max}], \qquad \Omega = D \times [0, T], \tag{2.1}$$

where x denotes rainfall intensity and y denotes the cumulative index. For $z \in \mathbb{R}$, write

$$z^+ = \max\{z, 0\}.$$

Under $\mathbb{P}$, rainfall intensity follows the seasonally forced Ornstein–Uhlenbeck equation

$$dX_t = \Big(k[\theta(t) - X_t] + \theta'(t)\Big)\,dt + \sigma\,dW_t, \qquad X_0 = x. \tag{2.2}$$

Mean-reverting dynamics of this type are standard in weather-derivative modelling; see, for example, [14,27]. Here $k > 0$ is the mean-reversion rate, $\sigma > 0$ is the volatility, and θ is the seasonal rainfall mean. The term $\theta'(t)$ keeps the deterministic trajectory on the moving seasonal level: if $\sigma = 0$ and $X_0 = \theta(0)$, then $X_t = \theta(t)$ for all t.

Let $X_{\text{ref}} \geq 0$ be a reference rainfall level. The deficit accumulation rate is

$$f(x) = (X_{\text{ref}} - x)^+. \tag{2.3}$$

The cumulative index satisfies

$$dY_t = f(X_t)\,dt, \qquad Y_0 = y. \tag{2.4}$$

Equivalently,

$$Y_t = y + \int_0^t (X_{\text{ref}} - X_s)^+\,ds.$$

The index grows only while rainfall intensity lies below the reference level.

The numerical study uses a put payoff written on the cumulative index,

$$\Phi(X_T, Y_T) = \text{tick}\,(K - Y_T)^+, \tag{2.5}$$

where $K \geq 0$ is the strike and tick > 0 is the monetary conversion factor. This convention is retained throughout the computations. A contract paying on large accumulated deficits would instead use $\text{tick}(Y_T - K)^+$. The pricing operator below is unchanged in that case; only the terminal and boundary data must be replaced.

Rainfall is not traded, so the pricing measure is specified rather than obtained from replication. Let $\lambda \in \mathbb{R}$ be constant and define

$$Z_t = \exp\Big(-\lambda W_t - \frac{1}{2}\lambda^2 t\Big), \qquad 0 \leq t \leq T. \tag{2.6}$$

Novikov's condition holds because λ is constant. Hence Z is a martingale, and the measure $\mathbb{Q}$ defined by

$$\frac{d\mathbb{Q}}{d\mathbb{P}}\bigg|_{\mathcal{F}_T} = Z_T \tag{2.7}$$

is equivalent to $\mathbb{P}$ on $\mathcal{F}_T$. By Girsanov's theorem,

$$W_t^{\mathbb{Q}} = W_t + \lambda t \tag{2.8}$$

is a Brownian motion under $\mathbb{Q}$. Substituting $dW_t = dW_t^{\mathbb{Q}} - \lambda\,dt$ into (2.2) gives

$$dX_t = \gamma(X_t, t)\,dt + \sigma\,dW_t^{\mathbb{Q}}, \qquad \gamma(x,t) = k[\theta(t) - x] + \theta'(t) - \lambda\sigma. \tag{2.9}$$

The finite-variation equation for Y_t is unchanged.

Let $r \geq 0$ denote the risk-free rate. The calendar-time value of the contract is

$$U(t, x, y) = \mathbb{E}^{\mathbb{Q}}\Big[e^{-r(T-t)}\Phi(X_T, Y_T)\,\Big|\,X_t = x,\ Y_t = y\Big]. \tag{2.10}$$

For a smooth test function $u(t, x, y)$, the generator of (X_t, Y_t) under $\mathbb{Q}$ is

$$\mathcal{A}u = \gamma(x,t)u_x + f(x)u_y + \frac{1}{2}\sigma^2 u_{xx}.$$

Itô's formula applied to $e^{-rt}u(t, X_t, Y_t)$ gives

$$d\left(e^{-rt}u(t, X_t, Y_t)\right) = e^{-rt}\left(u_t + \mathcal{A}u - ru\right)dt + e^{-rt}\sigma u_x\, dW_t^{\mathbb{Q}}.$$

For $u = U$, the discounted value process is a $\mathbb{Q}$-martingale. Hence

$$U_t + \mathcal{A}U - rU = 0, \qquad 0 \le t < T, \tag{2.11}$$

with terminal condition $U(T, x, y) = \Phi(x, y)$.

Set

$$V(x, y, \tau) = U(T - \tau, x, y).$$

Then $U_t = -V_\tau$. Writing

$$\gamma(x, \tau) := \gamma(x, T - \tau),$$

we obtain the backward-time pricing equation

$$V_\tau = \gamma(x,\tau)V_x + f(x)V_y + \frac{1}{2}\sigma^2 V_{xx} - rV, \qquad (x, y, \tau) \in D^\circ \times (0, T]. \tag{2.12}$$

For the payoff (2.5), the initial condition in backward time is

$$V(x, y, 0) = \mathrm{tick}(K - y)^+. \tag{2.13}$$

The boundary conditions follow from the truncation and the transport direction. At the dry boundary $x = x_{\min}$, the rainfall intensity is held fixed at the lowest level in the domain, so the index accumulates at rate $f(x_{\min})$. This gives

$$V(x_{\min}, y, \tau) = \mathrm{tick}\Big(K - [y + f(x_{\min})\tau]\Big)^+. \tag{2.14}$$

At the wet boundary $x = x_{\max}$, chosen so that $x_{\max} \ge X_{\mathrm{ref}}$, further increases in rainfall intensity do not increase the deficit rate. We impose the reflecting condition

$$V_x(x_{\max}, y, \tau) = 0. \tag{2.15}$$

Finally, for $y_{\max} > K$, the put payoff is zero at the upper index boundary, and we set

$$V(x, y_{\max}, \tau) = 0. \tag{2.16}$$

No boundary value is prescribed at $y = 0$, since the transport field in the backward-time equation points toward decreasing y when written in standard transport form. The imposed condition at $y = y_{\max}$ is the inflow condition for the truncated index domain.

The pricing problem is

$$\begin{cases} V_\tau = \gamma(x,\tau)V_x + f(x)V_y + \dfrac{1}{2}\sigma^2 V_{xx} - rV, & (x,y,\tau) \in D^\circ \times (0,T], \\ V(x,y,0) = \mathrm{tick}(K-y)^+, & (x,y) \in D, \\ V(x_{\min},y,\tau) = \mathrm{tick}\Big(K - [y + f(x_{\min})\tau]\Big)^+, & (y,\tau) \in [0,y_{\max}] \times [0,T], \\ V_x(x_{\max},y,\tau) = 0, & (y,\tau) \in [0,y_{\max}] \times [0,T], \\ V(x,y_{\max},\tau) = 0, & (x,\tau) \in [x_{\min},x_{\max}] \times [0,T]. \end{cases} \tag{2.17}$$

3. Analytical Properties of the Pricing Equation

We next study the basic analytical properties of (2.17). The equation is linear, but it is not uniformly parabolic in the two spatial variables. Diffusion appears only in the rainfall-intensity variable x; the accumulated index y is governed by first-order transport. This distinction is not cosmetic. It determines which boundary terms have a sign, where boundary data may be prescribed, and which quantities can be controlled by an energy estimate.

Assumption 3.1. *The coefficients and data in* (2.17) *satisfy the following conditions.*

(i) *The seasonal mean satisfies $\theta \in C^2([0,T])$, and*

$$k > 0, \qquad \sigma > 0, \qquad r \geq 0, \qquad \lambda \in \mathbb{R}.$$

(ii) *The drift*

$$\gamma(x,\tau) = k[\theta(T-\tau) - x] + \theta'(T-\tau) - \lambda\sigma$$

belongs to $C^1([x_{\min},x_{\max}] \times [0,T])$, and

$$\|\gamma\|_{L^\infty(\Omega)} < \infty, \qquad \|\gamma_x\|_{L^\infty(\Omega)} < \infty.$$

(iii) *The accumulation rate f is nonnegative and belongs to $W^{1,\infty}([x_{\min},x_{\max}])$. In the deficit model, $f(x) = (X_{\mathrm{ref}} - x)^+$.*

(iv) *The boundary and initial data are compatible at the corner points where the prescribed faces meet. For the kinked payoff* $\mathrm{tick}(K-y)^+$*, classical statements are understood by smooth monotone approximation and passage to the energy limit.*

Throughout this section,

$$D = [x_{\min},x_{\max}] \times [0,y_{\max}], \qquad \|u\| = \|u\|_{L^2(D)}.$$

The term that can weaken dissipation is the derivative of the drift in the diffusive direction. We therefore set

$$\mu := r - \frac{1}{2}\|\gamma_x\|_{L^\infty(\Omega)}.$$

The estimate below is written in the dissipative case $\mu > 0$. If $\mu \leq 0$, the same calculation gives a finite-time bound with the usual Gronwall factor. Nothing in the comparison or monotonicity arguments depends on exponential decay.

Theorem 3.1 (Energy estimate)**.** *Assume 3.1 and suppose $\mu > 0$. Let V be a smooth solution of the homogeneous version of* (2.17)*, with zero essential Dirichlet traces and with $V_x = 0$ on $x = x_{\max}$. Then, for every $0 \le \tau \le T$,*

$$\|V(\tau)\|^2 + \sigma^2 \int_0^\tau \|V_x(s)\|^2\, ds \le e^{-2\mu\tau}\|V(0)\|^2. \tag{3.1}$$

Proof. The proof is a direct energy calculation, but the signs of the transport boundary terms must be kept. Testing

$$V_\tau = \gamma V_x + f V_y + \frac{1}{2}\sigma^2 V_{xx} - rV$$

against V over D gives

$$\frac{1}{2}\frac{d}{d\tau}\|V(\tau)\|^2 = \int_D \gamma V V_x\, dxdy + \int_D f V V_y\, dxdy + \frac{1}{2}\sigma^2 \int_D V V_{xx}\, dxdy - r\|V(\tau)\|^2.$$

The diffusion term gives

$$\frac{1}{2}\sigma^2 \int_D V V_{xx}\, dxdy = \frac{1}{2}\sigma^2 \int_0^{y_{\max}} [V V_x]_{x_{\min}}^{x_{\max}}\, dy - \frac{1}{2}\sigma^2 \|V_x(\tau)\|^2.$$

The boundary contribution is zero because the homogeneous trace is imposed at $x = x_{\min}$ and $V_x = 0$ at $x = x_{\max}$. Thus diffusion contributes exactly

$$-\frac{1}{2}\sigma^2\|V_x(\tau)\|^2.$$

For the drift in x, integration by parts gives

$$\int_D \gamma V V_x\, dxdy = \frac{1}{2}\int_0^{y_{\max}} [\gamma V^2]_{x_{\min}}^{x_{\max}}\, dy - \frac{1}{2}\int_D \gamma_x V^2\, dxdy.$$

The homogeneous boundary setting is chosen so that the boundary contribution is nonpositive. Hence

$$\int_D \gamma V V_x\, dxdy \le \frac{1}{2}\|\gamma_x\|_{L^\infty(\Omega)}\|V(\tau)\|^2.$$

The y-transport term has a useful sign. Since $f = f(x)$,

$$\int_D f V V_y\, dxdy = \frac{1}{2}\int_{x_{\min}}^{x_{\max}} f(x)\left[V^2(x, y_{\max}, \tau) - V^2(x, 0, \tau)\right] dx.$$

The saturation boundary gives $V(x, y_{\max}, \tau) = 0$, and $f \ge 0$. Therefore

$$\int_D f V V_y\, dxdy = -\frac{1}{2}\int_{x_{\min}}^{x_{\max}} f(x) V^2(x, 0, \tau)\, dx \le 0.$$

Combining the three estimates, we obtain

$$\frac{1}{2}\frac{d}{d\tau}\|V(\tau)\|^2 + \frac{1}{2}\sigma^2\|V_x(\tau)\|^2 + \left(r - \frac{1}{2}\|\gamma_x\|_{L^\infty(\Omega)}\right)\|V(\tau)\|^2 \le 0.$$

By the definition of μ,

$$\frac{d}{d\tau}\|V(\tau)\|^2 + \sigma^2\|V_x(\tau)\|^2 + 2\mu\|V(\tau)\|^2 \le 0.$$

Multiplication by $e^{2\mu\tau}$ and integration over $[0, \tau]$ give (3.1). □

Corollary 3.1 (Continuous dependence on data)**.** *Let $V^{(1)}$ and $V^{(2)}$ solve* (2.17) *with the same coefficients and with initial and boundary data differing by $\Delta\Phi$ and ΔG. Then*

$$\|V^{(1)}(\tau) - V^{(2)}(\tau)\|^2 \le C_T \left(\|\Delta\Phi\|^2_{L^2(D)} + \|\Delta G\|^2_{\mathrm{tr}}\right), \qquad 0 \le \tau \le T,$$

where $\|\cdot\|_{\mathrm{tr}}$ is the trace norm of the prescribed boundary-data difference, and C_T depends only on the coefficient bounds, T, and the domain.

Proof. Let $Z = V^{(1)} - V^{(2)}$. Then Z satisfies the same differential operator with initial datum $\Delta\Phi$ and boundary discrepancy ΔG. Choose a lifting G with these traces and write $Z = W + G$, so that W has homogeneous essential traces. The equation for W contains the forcing term obtained by applying

$$\mathcal{P} = \partial_\tau - \gamma\partial_x - f\partial_y - \frac{1}{2}\sigma^2\partial_{xx} + r$$

to G. The trace theorem and the coefficient bounds give

$$\|G\|_{\mathcal{E}} + \|\mathcal{P}G\|_{L^2(0,T;H^{-1}(D))} \le C\|\Delta G\|_{\mathrm{tr}},$$

where $\mathcal{E}$ is the natural energy norm. Applying the preceding energy estimate to W, estimating the forcing by duality and Young's inequality, and then using Gronwall's inequality yields the claimed bound. If $\Delta\Phi = 0$ and $\Delta G = 0$, this estimate gives $Z = 0$, so uniqueness follows as a special case. □

Theorem 3.2 (Well-posedness)**.** *Assume 3.1. For compatible smooth initial and boundary data, the problem* (2.17) *admits a unique classical solution*

$$V \in C^{2,1}(D^\circ \times (0,T]) \cap C(\overline{D} \times [0,T]).$$

For the payoff $V(x,y,0) = \mathrm{tick}(K-y)^+$, the problem admits a unique energy solution obtained as the limit of smooth monotone payoff approximations. This solution satisfies the stability estimate of 3.1 after the nonhomogeneous boundary data are lifted.

Proof. We first treat smooth compatible data. Subtract a smooth lifting of the nonhomogeneous boundary conditions. The transformed equation has homogeneous essential traces and an inhomogeneous term in $L^2(0,T;H^{-1}(D))$. For test functions with the homogeneous essential traces, define

$$a_\tau(u,v) = \frac{1}{2}\sigma^2 \int_D u_x v_x \, dxdy - \int_D \gamma(x,\tau) u_x v \, dxdy - \int_D f(x) u_y v \, dxdy + r\int_D uv \, dxdy.$$

The coefficient bounds imply

$$|a_\tau(u,v)| \le C\|u\|_{H^1(D)}\|v\|_{H^1(D)}.$$

The lower-order terms are controlled by Young's inequality:

$$\left|\int_D \gamma u_x u \, dxdy\right| \le \varepsilon\|u_x\|^2 + C_\varepsilon\|u\|^2,$$

and

$$\left|\int_D f u_y u \, dxdy\right| \le \varepsilon \|u_y\|^2 + C_\varepsilon \|u\|^2.$$

After adding a sufficiently large multiple of $\|u\|^2$, the form satisfies a Gårding inequality on the homogeneous energy space. The standard variational construction for linear parabolic equations then gives a unique weak solution

$$V \in L^2(0,T;H^1(D)), \qquad V_\tau \in L^2(0,T;H^{-1}(D)).$$

For smooth coefficients and compatible data, interior parabolic regularity gives the stated classical regularity in $D^\circ \times (0,T]$, together with continuity up to the compatible parabolic boundary.

The payoff tick$(K-y)^+$ is not smooth at $y = K$. Choose smooth decreasing functions $\Phi^\varepsilon \in C^\infty([0,y_{\max}])$ such that

$$\Phi^\varepsilon \to \text{tick}(K-y)^+ \quad \text{uniformly on } [0,y_{\max}],$$

and choose compatible smooth boundary data for each Φ^ε. Let V^ε be the corresponding classical solution. The continuous-dependence estimate shows that $\{V^\varepsilon\}$ is Cauchy in the energy norm whenever the smoothed data are Cauchy in $L^2(D)$ and in the associated trace norm. Its limit is an energy solution of (2.17) with the kinked payoff. If two limits were possible, their difference would solve the homogeneous problem with zero data, and the energy estimate would force that difference to vanish. The energy solution is therefore unique. □

Proposition 3.1 (Comparison principle). *Let $V^{(1)}$ and $V^{(2)}$ be classical solutions of* (2.12) *with the same coefficients. Suppose*

$$V^{(1)}(x,y,0) \le V^{(2)}(x,y,0) \quad \text{on } D,$$

and suppose the same ordering holds on the prescribed boundary faces. Then

$$V^{(1)}(x,y,\tau) \le V^{(2)}(x,y,\tau) \quad \text{for all } (x,y,\tau) \in \overline{D} \times [0,T].$$

Proof. Put $Z = V^{(1)} - V^{(2)}$. Then

$$Z_\tau = \gamma Z_x + f Z_y + \frac{1}{2}\sigma^2 Z_{xx} - rZ$$

and the initial and prescribed boundary data for Z are nonpositive. To exclude a positive maximum in the interior, fix $\eta > 0$ and set

$$Z_\eta(x,y,\tau) = Z(x,y,\tau) - \eta\tau.$$

If Z_η attained a positive maximum at an interior point (x_0,y_0,τ_0) with $\tau_0 > 0$, then at that point

$$(Z_\eta)_\tau \ge 0, \qquad (Z_\eta)_x = 0, \qquad (Z_\eta)_y = 0, \qquad (Z_\eta)_{xx} \le 0.$$

Since $Z = Z_\eta + \eta\tau$, the equation gives

$$(Z_\eta)_\tau + \eta = \gamma (Z_\eta)_x + f(Z_\eta)_y + \frac{1}{2}\sigma^2 (Z_\eta)_{xx} - r(Z_\eta + \eta\tau) \le -rZ_\eta.$$

The left-hand side is at least η, while the right-hand side is nonpositive at a positive maximum. This contradiction rules out positive interior maxima. The ordered initial and boundary data rule out positive maxima on the parabolic boundary. Hence $Z_\eta \le 0$. Letting $\eta \downarrow 0$ gives $Z \le 0$. □

Corollary 3.2 (Positivity and payoff-scale bound)**.** *For the payoff* $\Phi(y) = \mathrm{tick}(K-y)^+$, *the solution of* (2.17) *satisfies*

$$0 \le V(x,y,\tau) \le \mathrm{tick}K \qquad \text{for all } (x,y,\tau) \in \overline{D} \times [0,T].$$

If all prescribed boundary data are discounted consistently, then the sharper bound

$$V(x,y,\tau) \le e^{-r\tau}\mathrm{tick}K$$

holds.

Proof. The zero function lies below the payoff and below the prescribed boundary data; the comparison principle therefore gives $V \ge 0$. The constant function tick$K$ is a supersolution because

$$(\mathrm{tick}K)_\tau - \gamma(\mathrm{tick}K)_x - f(\mathrm{tick}K)_y - \frac{1}{2}\sigma^2(\mathrm{tick}K)_{xx} + r\mathrm{tick}K = r\mathrm{tick}K \ge 0.$$

Since the payoff and boundary data are bounded above by tick$K$, another application of comparison gives $V \le \mathrm{tick}K$. If the prescribed data satisfy the corresponding discounted upper bound, the same argument with $e^{-r\tau}\mathrm{tick}K$ gives the sharper estimate. □

Proposition 3.2 (Monotonicity in the cumulative index)**.** *Let V be the solution of* (2.17)*. If* $0 \le y_1 \le y_2 \le y_{\max}$, *then*

$$V(x,y_1,\tau) \ge V(x,y_2,\tau)$$

for every $x \in [x_{\min}, x_{\max}]$ *and* $\tau \in [0,T]$*. In particular,* $V_y \le 0$ *wherever the derivative exists.*

Proof. Fix $h > 0$ and consider

$$Z_h(x,y,\tau) = V(x,y+h,\tau) - V(x,y,\tau), \qquad 0 \le y \le y_{\max} - h.$$

Because f depends only on x, the translated function $V(x,y+h,\tau)$ satisfies the same differential operator as $V(x,y,\tau)$. Thus Z_h solves the homogeneous pricing equation on the reduced cylinder. At $\tau = 0$,

$$Z_h(x,y,0) = \mathrm{tick}(K-y-h)^+ - \mathrm{tick}(K-y)^+ \le 0.$$

The dry-boundary data have the same order:

$$\mathrm{tick}\Big(K - [y+h+f(x_{\min})\tau]\Big)^+ - \mathrm{tick}\Big(K - [y+f(x_{\min})\tau]\Big)^+ \le 0.$$

At $y = y_{\max} - h$, the first term is evaluated at $y_{\max}$, where the saturation boundary is zero, while the second term is nonnegative. The remaining prescribed boundary faces preserve the same ordering. The comparison principle gives $Z_h \le 0$, hence

$$V(x,y+h,\tau) \le V(x,y,\tau).$$

Taking $h = y_2 - y_1$ proves the monotonicity assertion. The inequality $V_y \le 0$ follows at all points where the derivative exists. □

4. Numerical Methods

We use two approximations of (2.17). The finite-difference method gives a reference solution on a Cartesian grid. The residual-based approximation uses a smooth parametric trial function and penalizes the differential equation together with the prescribed data. The two methods serve different purposes: the grid method provides a controlled benchmark, while the residual formulation gives a mesh-free approximation whose error can be compared with the PDE residual.

4.1. **Finite-difference reference scheme.**

Let

$$x_i = x_{\min} + i\Delta x, \qquad y_j = j\Delta y, \qquad \tau^n = n\Delta\tau,$$

where

$$\Delta x = \frac{x_{\max} - x_{\min}}{N_x}, \qquad \Delta y = \frac{y_{\max}}{N_y}, \qquad \Delta\tau = \frac{T}{N_\tau}.$$

We write $V^n_{i,j}$ for the approximation of $V(x_i, y_j, \tau^n)$. The diffusion in x is discretised by

$$\delta_{xx} V^n_{i,j} = \frac{V^n_{i+1,j} - 2V^n_{i,j} + V^n_{i-1,j}}{\Delta x^2},$$

and the drift in x by

$$\delta^0_x V^n_{i,j} = \frac{V^n_{i+1,j} - V^n_{i-1,j}}{2\Delta x}.$$

Writing the PDE as

$$V_\tau - f(x)V_y = \gamma(x,\tau)V_x + \frac{1}{2}\sigma^2 V_{xx} - rV$$

shows that the transport speed in the y-direction is $-f(x)$. Since $f \geq 0$, the upwind derivative is the forward difference

$$\delta^+_y V^n_{i,j} = \frac{V^n_{i,j+1} - V^n_{i,j}}{\Delta y}.$$

This is the discretisation that uses the prescribed saturation boundary at $y = y_{\max}$ and avoids imposing an artificial condition at $y = 0$.

For $1 \leq i \leq N_x - 1$ and $0 \leq j \leq N_y - 1$, the reference update is

$$V^{n+1}_{i,j} = V^n_{i,j} + \Delta\tau\left[\gamma(x_i,\tau^n)\delta^0_x V^n_{i,j} + f(x_i)\delta^+_y V^n_{i,j} + \frac{1}{2}\sigma^2\delta_{xx} V^n_{i,j} - rV^n_{i,j}\right]. \tag{4.1}$$

The initial data are imposed by

$$V^0_{i,j} = \text{tick}(K - y_j)^+. \tag{4.2}$$

The boundary conditions are discretised as

$$V^n_{0,j} = \text{tick}\Big(K - [y_j + f(x_{\min})\tau^n]\Big)^+, \tag{4.3}$$

$$\frac{V^n_{N_x,j} - V^n_{N_x-1,j}}{\Delta x} = 0, \tag{4.4}$$

$$V^n_{i,N_y} = 0. \tag{4.5}$$

For the centred stencil at the wet boundary, the Neumann condition is implemented by the ghost-point relation

$$V^n_{N_x+1,j} = V^n_{N_x-1,j}.$$

Proposition 4.1 (Local truncation error). *Let V be a smooth solution of* (2.17) *away from the payoff kink, with all derivatives appearing below bounded on Ω. If $\mathcal{T}^n_{i,j}$ denotes the local truncation error obtained by inserting the exact solution into* (4.1)*, then*

$$|\mathcal{T}^n_{i,j}| \le C\left(\Delta\tau + \Delta x^2 + \Delta y\right), \tag{4.6}$$

where C is independent of the mesh widths.

Proof. At (x_i, y_j, τ^n),

$$\frac{V(x_i, y_j, \tau^{n+1}) - V(x_i, y_j, \tau^n)}{\Delta\tau} = V_\tau + \frac{\Delta\tau}{2} V_{\tau\tau} + O(\Delta\tau^2).$$

The centred differences in x give

$$\delta^0_x V = V_x + \frac{\Delta x^2}{6} V_{xxx} + O(\Delta x^4), \qquad \delta_{xx} V = V_{xx} + \frac{\Delta x^2}{12} V_{xxxx} + O(\Delta x^4),$$

while the upwind difference in y gives

$$\delta^+_y V = V_y + \frac{\Delta y}{2} V_{yy} + O(\Delta y^2).$$

After these expansions are substituted into (4.1), the leading terms cancel against

$$V_\tau - \gamma V_x - f V_y - \frac{1}{2}\sigma^2 V_{xx} + rV = 0.$$

The remaining terms have size at most $C(\Delta\tau + \Delta x^2 + \Delta y)$, with C depending on the relevant derivatives of V, the coefficient bounds, and the domain, but not on the mesh widths. □

The explicit scheme uses a centred approximation of the x-drift. The time step must therefore control diffusion, transport, and drift. The next condition is only a sufficient stability condition.

Set

$$F_{\max} := \max_{x \in [x_{\min}, x_{\max}]} f(x), \qquad \Gamma_{\max} := \max_{(x,\tau) \in [x_{\min}, x_{\max}] \times [0,T]} |\gamma(x, \tau)|.$$

If $F_{\max} = 0$ or $\Gamma_{\max} = 0$, the corresponding restriction below is omitted.

Theorem 4.1 (Sufficient stability condition). *Assume $f \ge 0$, $\sigma > 0$, and $\gamma \in L^\infty(\Omega)$. There exists a constant $C_{\mathrm{CFL}} > 0$, depending only on fixed bounds for the coefficients, such that if*

$$\Delta\tau \le C_{\mathrm{CFL}} \min\left\{\frac{\Delta x^2}{\sigma^2}, \frac{\Delta y}{F_{\max}}, \frac{\sigma^2}{\Gamma^2_{\max}}\right\}, \tag{4.7}$$

then the homogeneous update associated with (4.1) *is stable in the discrete ℓ^2-norm on every finite time interval. More precisely, there is $C_T > 0$, independent of the mesh widths, such that*

$$\|V^n\|_{\ell^2} \le C_T \|V^0\|_{\ell^2}, \qquad n\Delta\tau \le T.$$

Proof. The proof is local in the coefficients; the variable-coefficient estimate follows by taking the bounds $F_{\max}$ and $\Gamma_{\max}$. Consider first the constant-coefficient interior scheme. For the Fourier mode

$$V_{i,j}^n = A^n e^{\mathrm{i}(\xi i+\eta j)}, \qquad \xi, \eta \in [-\pi, \pi],$$

the amplification factor is

$$G(\xi,\eta) = 1 - 4c\sin^2\frac{\xi}{2} + a(e^{\mathrm{i}\eta} - 1) + 2\mathrm{i}b\sin\xi - \delta,$$

with

$$c = \frac{\sigma^2\Delta\tau}{2\Delta x^2}, \qquad a = \frac{f\Delta\tau}{\Delta y}, \qquad b = \frac{\gamma\Delta\tau}{2\Delta x}, \qquad \delta = r\Delta\tau.$$

The discount term can only add damping, so it suffices to estimate the remaining factor. Put

$$S = \sin^2\frac{\xi}{2}, \qquad C = 1 - \cos\eta.$$

Then

$$G = 1 - 4cS - aC + \mathrm{i}(a\sin\eta + 2b\sin\xi).$$

Since $\sin^2\eta \le 2C$ and $\sin^2\xi \le 4S$,

$$\begin{aligned} |G|^2 &= (1-4cS-aC)^2 + (a\sin\eta + 2b\sin\xi)^2 \\ &\le (1-4cS-aC)^2 + 2a^2\sin^2\eta + 8b^2\sin^2\xi \\ &\le (1-4cS-aC)^2 + 4a^2C + 32b^2S. \end{aligned}$$

For a, c, and b^2/c sufficiently small, the damping $4cS + aC$ controls the quadratic terms. The restrictions

$$a \le a_0, \qquad c \le c_0, \qquad b^2 \le \kappa c$$

with fixed small $a_0, c_0, \kappa > 0$ are implied by (4.7) after reducing C_{CFL}. Thus

$$|G(\xi,\eta)| \le 1 + C\Delta\tau$$

uniformly in ξ and η, and iteration gives

$$|A|^n \le (1 + C\Delta\tau)^n \le e^{CT}, \qquad n\Delta\tau \le T.$$

Parseval's identity gives the same bound in the discrete ℓ^2-norm. The homogeneous Dirichlet faces are dissipative, and the Neumann ghost-point closure is energy-neutral for the discrete diffusion operator. The finite-time estimate follows. □

Theorem 4.2 (Finite-difference convergence)**.** *Let the hypotheses of 4.1 and 4.1 hold, and assume the boundary data are compatible at the grid corners. If V_h denotes the finite-difference solution generated by* (4.1)*, then, for $n\Delta\tau \le T$,*

$$\|V_h^n - V(\tau^n)\|_{\ell^2} \le C_T\left(\Delta\tau + \Delta x^2 + \Delta y\right), \tag{4.8}$$

where C_T is independent of the mesh widths.

Proof. Let V^n be the exact solution sampled on the grid and set

$$E^n = V_h^n - V^n.$$

When the exact solution is inserted into the scheme,

$$V^{n+1} = \mathcal{S}_h V^n + \Delta\tau\,\mathcal{T}^n,$$

where $\mathcal{S}_h$ is the homogeneous one-step operator. The computed solution satisfies

$$V_h^{n+1} = \mathcal{S}_h V_h^n.$$

Thus

$$E^{n+1} = \mathcal{S}_h E^n - \Delta\tau\,\mathcal{T}^n.$$

By stability,

$$\|E^{n+1}\|_{\ell^2} \le (1 + C\Delta\tau)\|E^n\|_{\ell^2} + \Delta\tau\|\mathcal{T}^n\|_{\ell^2}.$$

The initial data are imposed exactly, hence $E^0 = 0$. Iteration gives

$$\|E^n\|_{\ell^2} \le \sum_{m=0}^{n-1} (1 + C\Delta\tau)^{n-1-m} \Delta\tau\,\|\mathcal{T}^m\|_{\ell^2}.$$

For $n\Delta\tau \le T$, the factor

$$(1 + C\Delta\tau)^{n-1-m}$$

is bounded by e^{CT}. Using (4.6), we obtain

$$\|E^n\|_{\ell^2} \le C_T(\Delta\tau + \Delta x^2 + \Delta y),$$

which proves (4.8). □

4.2. **Residual-based parametric approximation.** Let $V_\theta : \Omega \to \mathbb{R}$ be a smooth parametric trial function. In the computations V_θ is a fully connected neural network with smooth activation, but the estimate below only uses differentiability and evaluation of the derivatives in the operator. Define

$$\mathcal{R}_\theta(x, y, \tau) = (V_\theta)_\tau - \gamma(x, \tau)(V_\theta)_x - f(x)(V_\theta)_y - \frac{1}{2}\sigma^2(V_\theta)_{xx} + rV_\theta. \tag{4.9}$$

The initial and boundary discrepancies are

$$\mathcal{I}_\theta(x, y) = V_\theta(x, y, 0) - \text{tick}(K - y)^+,$$

$$\mathcal{B}_\theta^{\min}(y, \tau) = V_\theta(x_{\min}, y, \tau) - \text{tick}\Big(K - [y + f(x_{\min})\tau]\Big)^+,$$

$$\mathcal{B}_\theta^{\max}(y, \tau) = (V_\theta)_x(x_{\max}, y, \tau), \qquad \mathcal{B}_\theta^{y}(x, \tau) = V_\theta(x, y_{\max}, \tau).$$

For collocation sets $C_r, C_0, C_{\min}, C_{\max}$, and C_y, the empirical loss is

$$\begin{aligned}\mathcal{J}(\theta) = w_r \frac{1}{|C_r|}\sum_{z\in C_r} |\mathcal{R}_\theta(z)|^2 + w_0 \frac{1}{|C_0|}\sum_{(x,y)\in C_0} |\mathcal{I}_\theta(x,y)|^2 \\ + w_{\min}\frac{1}{|C_{\min}|}\sum_{(y,\tau)\in C_{\min}} |\mathcal{B}_\theta^{\min}(y,\tau)|^2 + w_{\max}\frac{1}{|C_{\max}|}\sum_{(y,\tau)\in C_{\max}} |\mathcal{B}_\theta^{\max}(y,\tau)|^2 \\ + w_y \frac{1}{|C_y|}\sum_{(x,\tau)\in C_y} |\mathcal{B}_\theta^{y}(x,\tau)|^2.\end{aligned} \tag{4.10}$$

Architecture, sampling counts, optimisation settings, and hardware details are reported in Appendix A.

Theorem 4.3 (Residual-to-error estimate)**.** *Let V be the energy solution of* (2.17)*, and let V_θ be a smooth trial function. Set $e_\theta = V_\theta - V$. Then, for $0 \le \tau \le T$,*

$$\begin{aligned}\|e_\theta(\tau)\|^2_{L^2(D)} + \sigma^2\int_0^\tau \|(e_\theta)_x(s)\|^2_{L^2(D)}\,ds \le C_T\Big(\|\mathcal{I}_\theta\|^2_{L^2(D)} + \|\mathcal{B}_\theta^{\min}\|^2_{L^2(\Gamma^T_{\min})} \\ + \|\mathcal{B}_\theta^{\max}\|^2_{L^2(\Gamma^T_{\max})} + \|\mathcal{B}_\theta^{y}\|^2_{L^2(\Gamma^T_{y_{\max}})} \\ + \|\mathcal{R}_\theta\|^2_{L^2(0,T;H^{-1}(D))}\Big),\end{aligned} \tag{4.11}$$

where C_T depends on coefficient bounds, T, and the domain, but not on V_θ.

Proof. The error e_θ satisfies

$$(e_\theta)_\tau - \gamma(e_\theta)_x - f(e_\theta)_y - \frac{1}{2}\sigma^2(e_\theta)_{xx} + re_\theta = \mathcal{R}_\theta.$$

First assume that all initial and boundary discrepancies vanish. Testing this equation by e_θ and using the energy identity from 3.1 gives

$$\frac{1}{2}\frac{d}{d\tau}\|e_\theta(\tau)\|^2 + \frac{1}{2}\sigma^2\|(e_\theta)_x(\tau)\|^2 + \mu\|e_\theta(\tau)\|^2 \le \langle \mathcal{R}_\theta(\tau), e_\theta(\tau)\rangle_{H^{-1},H^1}.$$

The right-hand side is estimated by

$$|\langle \mathcal{R}_\theta, e_\theta\rangle| \le \|\mathcal{R}_\theta\|_{H^{-1}(D)}\|e_\theta\|_{H^1(D)}.$$

With homogeneous essential traces, the energy norm controls the quantity needed in the dual pairing. Hence, for every $\varepsilon > 0$,

$$|\langle \mathcal{R}_\theta, e_\theta\rangle| \le \varepsilon\sigma^2\|(e_\theta)_x\|^2 + \varepsilon\|e_\theta\|^2 + C_\varepsilon\|\mathcal{R}_\theta\|^2_{H^{-1}(D)}.$$

Choosing ε small gives

$$\frac{d}{d\tau}\|e_\theta(\tau)\|^2 + \sigma^2\|(e_\theta)_x(\tau)\|^2 \le C\|e_\theta(\tau)\|^2 + C\|\mathcal{R}_\theta(\tau)\|^2_{H^{-1}(D)}.$$

Gronwall's inequality proves the estimate in the homogeneous case.

For nonzero discrepancies, choose a lifting G_θ with traces

$$\mathcal{I}_\theta, \qquad \mathcal{B}_\theta^{\min}, \qquad \mathcal{B}_\theta^{\max}, \qquad \mathcal{B}_\theta^{y},$$

and write $e_\theta = w_\theta + G_\theta$. The function w_θ has homogeneous traces. The trace theorem bounds the lifting by the four discrepancy norms in (4.11). Applying the homogeneous estimate to w_θ, with forcing $\mathcal{R}_\theta + \mathcal{P}G_\theta$, gives (4.11). □

Proposition 4.2 (Error decomposition at maturity)**.** *Assume the hypotheses of 4.2 and 4.3. Suppose that the empirical sums in* (4.10) *form consistent quadrature rules for the corresponding continuous norms. Then, at* $\tau = T$*,*

$$\frac{\|V_\theta(T) - V_h(T)\|_{L^2(D)}}{\|V_h(T)\|_{L^2(D)}} \le C_1(\Delta\tau + \Delta x^2 + \Delta y) + C_2\mathcal{J}(\theta)^{1/2}, \tag{4.12}$$

where $C_1, C_2 > 0$ *are independent of* $h = (\Delta x, \Delta y, \Delta\tau)$ *and of the network parameters.*

Proof. Let V be the exact solution. At maturity,

$$V_\theta(T) - V_h(T) = [V_\theta(T) - V(T)] - [V_h(T) - V(T)].$$

Therefore

$$\|V_\theta(T) - V_h(T)\|_{L^2(D)} \le \|V_\theta(T) - V(T)\|_{L^2(D)} + \|V_h(T) - V(T)\|_{L^2(D)}.$$

The finite-difference term is controlled by 4.2. The residual term is controlled by 4.3. Consistency of the quadrature rules in (4.10) converts the continuous residual and boundary norms into a constant multiple of $\mathcal{J}(\theta)^{1/2}$. Since the contract is nontrivial, $\|V(T)\|_{L^2(D)} > 0$, and finite-difference convergence gives

$$\|V_h(T)\|_{L^2(D)} \ge \frac{1}{2}\|V(T)\|_{L^2(D)}$$

for all sufficiently fine meshes. Division by this lower bound proves (4.12), after absorbing constants. □

5. Rainfall Data and Calibration

The coefficients in the pricing equation are obtained from monthly rainfall observations. We separate the calibration into two parts: a deterministic seasonal mean and a stochastic mean-reverting anomaly. The fitted seasonal mean enters the drift through $\theta_c(t)$ and $\theta_c'(t)$, while the deseasonalised anomalies determine the mean-reversion rate and volatility.

5.1. **Rainfall data and preprocessing.** For each city

$$c \in \{\text{Riyadh}, \text{Jeddah}, \text{Makkah}, \text{Medina}, \text{Dammam}, \text{Abha}, \text{Tabuk}\},$$

let

$$R_m^{(c)}, \qquad m = 1, \ldots, M_c,$$

denote the observed monthly rainfall totals, measured in millimetres.

The calibration uses monthly observations directly, so no daily-to-monthly aggregation is performed. Missing entries are omitted from the least-squares fits. Extreme rainfall values are retained unless they are identified as recording errors, since unusually dry and wet months affect the cumulative rainfall-deficit index and hence the derivative value.

All rainfall variables in the calibration are measured in millimetres per month. The seven cities are chosen to represent arid interior, coastal, transitional inland, and high-rainfall southwestern regimes within Saudi Arabia.

5.2. **Seasonal rainfall mean.** The deterministic seasonal mean is represented by the periodic function

$$\theta_c(t) = a_0^{(c)} + \sum_{\ell=1}^{2} \beta_\ell^{(c)} \cos\left(\frac{2\pi\ell(t-\nu^{(c)})}{12}\right), \qquad t \in [0,12]. \tag{5.1}$$

The coefficients are estimated by nonlinear least squares:

$$\left(\widehat{a}_0^{(c)}, \widehat{\beta}_1^{(c)}, \widehat{\beta}_2^{(c)}, \widehat{\nu}^{(c)}\right) = \arg\min \sum_{m\in\mathcal{M}_c} \left[R_m^{(c)} - a_0 - \sum_{\ell=1}^{2} \beta_\ell \cos\left(\frac{2\pi\ell(t_m-\nu)}{12}\right)\right]^2. \tag{5.2}$$

Differentiating (5.1) gives

$$\theta_c'(t) = -\sum_{\ell=1}^{2} \beta_\ell^{(c)} \frac{2\pi\ell}{12} \sin\left(\frac{2\pi\ell(t-\nu^{(c)})}{12}\right). \tag{5.3}$$

TABLE 1. Calibrated Fourier coefficients for the seasonal rainfall mean $\theta_c(t)$.

City	a_0	β_1	β_2	ν
Riyadh	8.2	3.1	0.9	0.35
Jeddah	61.5	28.2	1.7	0.48
Makkah	55.0	22.0	2.5	0.45
Medina	47.0	18.5	2.1	0.44
Dammam	15.5	6.2	1.1	0.42
Abha	90.0	33.0	2.0	0.50
Tabuk	20.0	8.0	1.5	0.40

The fitted coefficients show the expected separation of regimes. Abha has the largest seasonal mean and amplitude. Riyadh and Tabuk have substantially lower seasonal rainfall levels. Jeddah, Makkah, and Medina lie between these two extremes.

5.3. **Mean-reversion and volatility estimation.** After the seasonal component has been removed, the anomalies are

$$Z_m^{(c)} = R_m^{(c)} - \widehat{\theta}_c(t_m). \tag{5.4}$$

For monthly observations, $\Delta t = 1$. The exact discrete transition of the Ornstein–Uhlenbeck anomaly process is

$$Z_{m+1}^{(c)} = \phi_c Z_m^{(c)} + \varepsilon_{m+1}^{(c)}, \qquad \phi_c = e^{-k_c\Delta t}.$$

The least-squares estimator of ϕ_c is

$$\widehat{\phi}_c = \frac{\sum_m Z_m^{(c)} Z_{m+1}^{(c)}}{\sum_m (Z_m^{(c)})^2}, \tag{5.5}$$

and the mean-reversion estimate is

$$\widehat{k}_c = -\frac{1}{\Delta t} \log(\widehat{\phi}_c). \tag{5.6}$$

The innovation variance satisfies

$$\mathrm{Var}(\varepsilon_{m+1}^{(c)}) = \frac{\sigma_c^2}{2k_c}\left(1 - e^{-2k_c \Delta t}\right).$$

Thus, if $\widehat{s}_c^2$ denotes the sample variance of the fitted innovations, then

$$\widehat{\sigma}_c = \left[\frac{2\widehat{k}_c \widehat{s}_c^2}{1 - e^{-2\widehat{k}_c \Delta t}}\right]^{1/2}. \tag{5.7}$$

5.4. **Financial inputs and contract specification.** Rainfall is not traded, so the market price of rainfall risk is not identified by replication. We therefore use a fixed city-specific value λ_c in the benchmark calculations and examine parameter sensitivity separately.

The annual risk-free rate is

$$r_{\text{annual}} = 0.05.$$

Since the pricing equation is solved in monthly time units, we use

$$r_{\text{month}} = \frac{r_{\text{annual}}}{12}. \tag{5.8}$$

The numerical experiments use the payoff

$$\Phi_c(Y_T) = \text{tick}_c (K_c - Y_T)^+,$$

with the reference rainfall level $X_{\text{ref},c}$, strike K_c, and maturity T listed in Table 2.

TABLE 2. Calibrated model parameters and contract specifications.

City	k	σ	λ	r	X_{ref}	K	T
Riyadh	0.65	4.8	0.10	0.05	30	31	12
Jeddah	0.72	8.2	0.12	0.05	60	65	12
Makkah	0.70	7.5	0.10	0.05	55	60	12
Medina	0.68	6.3	0.09	0.05	45	50	12
Dammam	0.62	5.0	0.08	0.05	25	30	12
Abha	0.80	9.0	0.11	0.05	85	90	12
Tabuk	0.60	4.5	0.07	0.05	20	25	12

The calibrated parameters vary substantially across the seven cities. Abha has the largest volatility and the fastest mean reversion. Riyadh and Tabuk have the smallest volatility estimates, consistent with arid interior conditions. Jeddah, Makkah, and Medina have larger seasonal rainfall levels and therefore larger reference values and strikes.

6. Numerical Validation

This section compares the residual-based approximation with the finite-difference reference solver. The validation is deliberately restricted to this comparison: both methods solve the same pricing equation, use the same calibrated parameters, and impose the same boundary and initial data.

For each city, the finite-difference solution is computed on a uniform Cartesian grid in (x, y, τ). The residual-based approximation is then evaluated on the same spatial grid at maturity. The relative discrepancy is measured by

$$\varepsilon_{L^2} = \frac{\left\| V_\theta(\cdot,\cdot,T) - V_{\mathrm{FD}}(\cdot,\cdot,T) \right\|_{L^2(D)}}{\left\| V_{\mathrm{FD}}(\cdot,\cdot,T) \right\|_{L^2(D)}}. \tag{6.1}$$

Here V_{FD} denotes the finite-difference reference solution and V_θ denotes the residual-based approximation.

Table 3. Final loss values and relative L^2-errors between the residual-based approximation and the finite-difference benchmark.

City	Total loss	PDE loss	Relative L^2 error
Riyadh	8.67×10^{-2}	5.36×10^{-2}	2.60×10^{-2}
Jeddah	6.38×10^{-1}	3.68×10^{-1}	4.53×10^{-2}
Makkah	4.95×10^{-1}	2.68×10^{-1}	8.56×10^{-2}
Medina	2.07×10^{-1}	1.19×10^{-1}	3.43×10^{-2}
Dammam	1.09×10^{-1}	4.00×10^{-2}	3.07×10^{-2}
Abha	1.41×10^{0}	9.38×10^{-1}	7.58×10^{-2}
Tabuk	8.61×10^{-2}	4.77×10^{-2}	2.72×10^{-2}

The relative errors in Table 3 remain below 9×10^{-2} for all seven cities. Riyadh and Tabuk give the smallest discrepancies, 2.60×10^{-2} and 2.72×10^{-2}, respectively. These cases have comparatively low calibrated volatility and smoother price surfaces. The largest discrepancy occurs in Makkah, where the value surface develops stronger curvature near the payoff transition; Abha also produces a larger error, consistent with its larger volatility and stronger seasonal level.

The table also shows that the PDE component is the dominant part of the final loss in each city. This behaviour is consistent with the residual-to-error estimate in Theorem 4.3: the approximation error is controlled by the residual together with the boundary and initial discrepancies. The benchmark therefore supports the use of the residual-based approximation as a numerical surrogate for the finite-difference reference solution on the calibrated domains.

7. Regional Case Studies

The calibrated cities represent distinct rainfall regimes rather than seven unrelated numerical tests. We therefore discuss the results by climatic structure: arid interior stations, coastal stations, transitional inland stations, and the high-rainfall southwest. The benchmark errors in Table 3 measure numerical agreement between the two solvers, while the figures in this section show representative price surfaces at maturity.

7.1. **Arid interior stations.** Riyadh and Tabuk have the smallest calibrated rainfall volatilities in Table 2. Their price surfaces are correspondingly smooth, and the residual-based approximation agrees closely with the finite-difference benchmark:

$$\varepsilon_{L^2} = 2.60 \times 10^{-2} \quad \text{for Riyadh}, \qquad \varepsilon_{L^2} = 2.72 \times 10^{-2} \quad \text{for Tabuk}.$$

The low errors reflect the mild curvature of the pricing surface in the rainfall-intensity direction. For these cities, most of the variation in the contract value comes from the accumulated index y, not from sharp changes in x.

Figure 1 shows Riyadh as the representative arid-interior case. The finite-difference and residual-based surfaces agree across the main valuation region. The largest pointwise discrepancies occur near the payoff transition, where the initial kink at $y = K$ leaves a visible numerical trace.

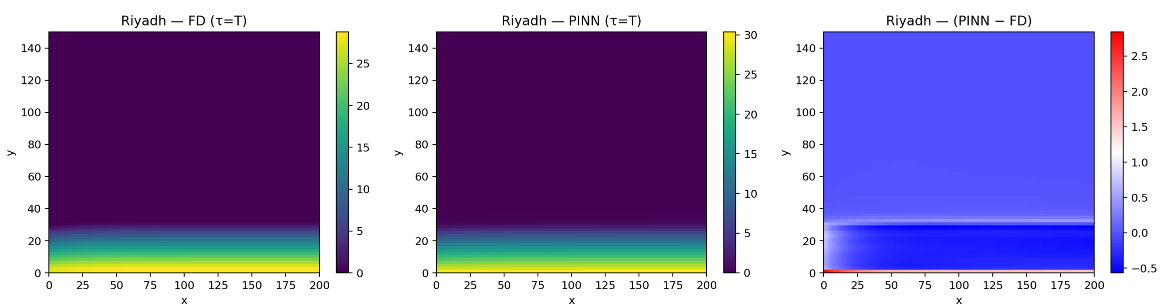

Figure 1. Riyadh: finite-difference price, residual-based price, and pointwise difference at $\tau = T$.

7.2. **Coastal stations.** Jeddah and Dammam are both coastal cities, but their calibrated parameters produce different levels of pricing variability. Jeddah has larger seasonal rainfall and higher volatility than Dammam, and this is reflected in the benchmark errors:

$$\varepsilon_{L^2} = 4.53 \times 10^{-2} \quad \text{for Jeddah}, \qquad \varepsilon_{L^2} = 3.07 \times 10^{-2} \quad \text{for Dammam}.$$

The Jeddah surface is broader and more curved than the arid-interior surfaces, whereas Dammam remains closer to the low-volatility cases.

Figure 2 gives the representative coastal surface. The residual-based approximation captures the main geometry of the finite-difference solution, including the flattening in wet regions where the deficit accumulation rate is small. The remaining discrepancy is concentrated in transition regions rather than in the saturated part of the domain.

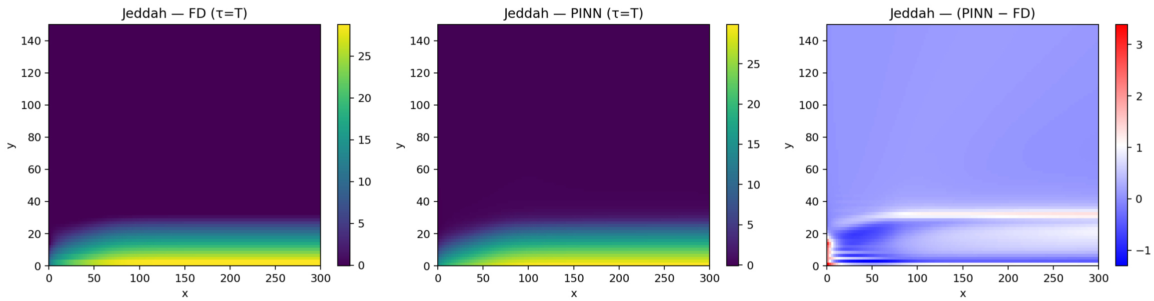

FIGURE 2. Jeddah: finite-difference price, residual-based price, and pointwise difference at $\tau = T$.

7.3. **Transitional inland stations.** Makkah and Medina form the main transitional inland group. Their rainfall levels are higher than those of the arid interior but lower than Abha's highland regime. Makkah is the most demanding case numerically:

$$\varepsilon_{L^2} = 8.56 \times 10^{-2}.$$

Medina has a smaller error,

$$\varepsilon_{L^2} = 3.43 \times 10^{-2}.$$

The difference between these two cities is consistent with the stronger curvature observed for Makkah. In this regime the value surface is shaped by the interaction between the payoff threshold, seasonal mean rainfall, and stochastic volatility.

Figure 3 displays the representative transitional case. The error is larger than in Riyadh or Jeddah, but it remains below 9×10^{-2} in relative L^2-norm. The concentration of the discrepancy near transition zones is expected: both the finite-difference discretisation and the residual-based approximation must resolve the kink inherited from tick$(K - y)^+$.

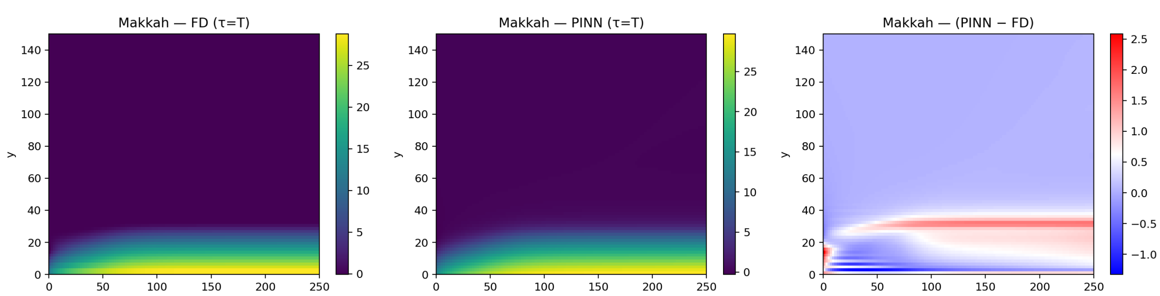

FIGURE 3. Makkah: finite-difference price, residual-based price, and pointwise difference at $\tau = T$.

7.4. **Orographic southwest.** Abha is separated from the other cities by its high seasonal rainfall level and larger calibrated volatility. These parameters produce a price surface governed by saturation effects: in many states the cumulative deficit is already far enough from the payoff-producing region that the put value is small. The residual-based approximation still reproduces the finite-difference benchmark with

$$\varepsilon_{L^2} = 7.58 \times 10^{-2},$$

but the final total loss is the largest among the seven cities. This is consistent with the stronger seasonal forcing and higher volatility reported in Tables 1 and 2.

Figure 4 shows the Abha surface. The qualitative structure remains correct: the value is non-negative, bounded by the payoff scale, and decreasing in the cumulative index, in agreement with Corollary 3.2 and Proposition 3.2. The larger residual error arises from the same transition and saturation regions that determine the financial interpretation of this high-rainfall case.

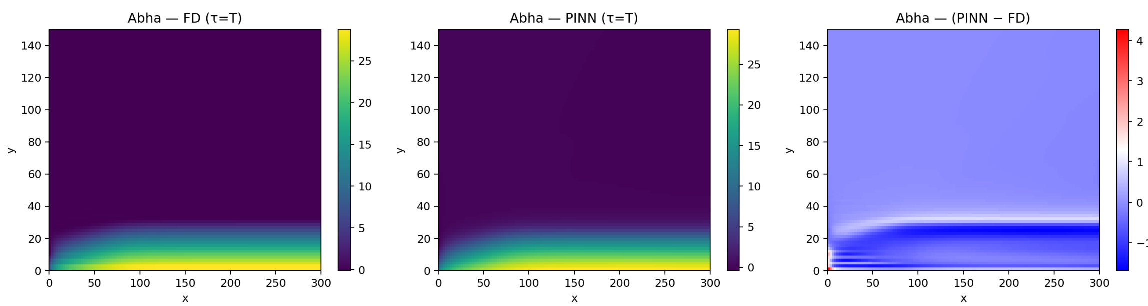

Figure 4. Abha: finite-difference price, residual-based price, and pointwise difference at $\tau = T$.

7.5. **Regional synthesis.** The regime comparison gives a clearer picture than a city-by-city listing. Arid interior stations have smooth surfaces and small benchmark errors. Coastal stations show broader pricing regions, with Jeddah more sensitive to rainfall variability than Dammam. Transitional inland stations display sharper transition layers, with Makkah giving the largest relative discrepancy. Abha is governed by a different mechanism: the high-rainfall regime pushes the deficit-index put toward saturation and changes the sign of several sensitivities discussed in Section 8.

These distinctions matter for contract design. The same payoff convention does not have the same financial character in every rainfall regime. In arid and transitional regions, the contract value is shaped by the probability of remaining near the deficit threshold. In the high-rainfall southwest, the same put payoff can lose value when the rainfall process is pulled toward wetter states. City-specific calibration is therefore not a numerical preference; it is required by the structure of the pricing problem.

8. Sensitivity Analysis

The calibrated parameters describe present rainfall conditions, but derivative values also depend on how the rainfall dynamics respond to parameter changes. This section examines the sensitivity of the mean contract value to perturbations in the mean-reversion rate k, volatility σ, and discount rate r.

Let $\overline{V}$ denote the average contract value over a fixed evaluation grid $G \subset D$. For a parameter $p \in \{k, \sigma, r\}$, the sensitivity measure is defined by

$$S_p = \frac{\overline{V}^{(p)} - \overline{V}}{\overline{V}}, \tag{8.1}$$

where $\overline{V}^{(p)}$ is computed after increasing p by 20% while all remaining parameters are held fixed.

Table 4. Sensitivity of the mean contract value to a 20% increase in the mean-reversion rate k, volatility σ, and discount rate r.

City	S_k	S_σ	S_r
Riyadh	+1.21%	−0.19%	−4.25%
Jeddah	+2.22%	+2.06%	+1.52%
Makkah	+8.27%	+9.89%	+9.86%
Medina	+3.14%	+3.70%	+4.50%
Dammam	+1.23%	+0.36%	+2.33%
Abha	−6.03%	−11.77%	−9.99%
Tabuk	+3.33%	+1.82%	−3.65%

The results in Table 4 show that the response of the contract value depends strongly on the rainfall regime. Makkah exhibits the largest positive sensitivities with respect to all three parameters. A 20% increase in volatility produces an increase of almost 10% in the mean contract value, indicating that the payoff remains strongly influenced by fluctuations around the deficit threshold. Medina displays the same qualitative behaviour, although with smaller magnitudes.

The arid interior cities respond more moderately. Riyadh and Tabuk exhibit relatively weak dependence on volatility, while their responses to the discount rate are negative. In these regions the value surface is already concentrated near low-payoff states, so moderate parameter changes produce comparatively small shifts in the expected payoff.

Abha differs from all other cities. The sensitivities are negative for each parameter:

$$(S_k, S_\sigma, S_r) = (-6.03\%, -11.77\%, -9.99\%).$$

This behaviour is consistent with the high-rainfall regime identified in Section 7. Faster mean reversion and larger volatility both increase the tendency of the process to revisit wetter states, reducing the probability of producing a positive payoff under the deficit-index put contract.

Taken together, the results indicate that parameter sensitivity is governed primarily by climatic regime rather than geographical location. Contracts calibrated to arid, transitional, and high-rainfall regions respond differently to the same perturbation. Stress testing therefore cannot rely on a single national parameter scenario; it must be performed within the rainfall regime for which the contract is intended.

9. Discussion and Conclusion

The valuation problem studied here is governed by one structural fact: the cumulative rainfall index is transported, not diffused. This affects every part of the analysis. It determines why the upper index boundary $y = y_{\max}$ is prescribed, why the finite-difference method uses a forward difference in y, and why the residual loss must penalize the boundary and initial discrepancies together with the PDE residual. Treating the index variable as if it were another diffusive state would give the wrong boundary problem.

The analytical results give simple tests for the computed prices. The solution is nonnegative, bounded by the payoff scale, and nonincreasing in the cumulative index. These properties are consequences of the comparison principle and the transport direction. They also have numerical value: a computed surface that violates any of them is not merely inaccurate; it is inconsistent with the pricing equation.

The benchmark comparison supports the residual-based approximation on the calibrated domains. The relative L^2-errors stay below 9×10^{-2} across all seven cities. The smaller errors in Riyadh and Tabuk are consistent with their lower calibrated volatility and smoother value surfaces. Makkah and Abha are more demanding cases. In Makkah the error is concentrated near the payoff transition, while in Abha the high seasonal rainfall level changes the shape of the value surface and increases the residual loss.

The regional study also shows why calibration cannot be separated from contract design. Arid interior cities have weak volatility exposure. Makkah and Medina respond more strongly to perturbations of mean reversion and volatility. Abha has negative sensitivities under the put payoff convention because the process is pulled toward wetter states where the payoff is smaller. This sign change is not a numerical anomaly. It follows from the interaction between the high seasonal rainfall level and a payoff that decreases with the cumulative index.

Several modelling choices should be kept in view. A single Gaussian mean-reverting factor captures seasonality and short memory, but it cannot represent storm clustering, persistent dry spells, or abrupt rainfall extremes. Those features would require a different rainfall dynamics, such as jump terms, regime switching, stochastic volatility, or spatial factors. The market price of rainfall risk is also imposed rather than inferred from liquid traded instruments. In applications it should therefore be treated as a risk-loading parameter and tested over a range of plausible values.

The numerical method has the same limitation as the model: its accuracy is tied to the parts of the domain where the contract is sensitive. The largest discrepancies occur near payoff transitions and boundary layers. Future computations should concentrate samples near $y = K$, near the dry boundary, and in regions where the finite-difference solution has large curvature. This is a more targeted improvement than simply increasing the number of collocation points.

The main conclusion is that rainfall-index derivatives require a regime-specific pricing analysis. The parabolic–transport formulation gives the mathematical structure, the finite-difference solver gives a benchmark, and the residual-based approximation gives a flexible surrogate. The Saudi case study shows that the same payoff can behave quite differently across rainfall regimes. For such contracts, regional calibration is part of the pricing model itself.

Appendix A. PINN Hyperparameters

This appendix records the numerical settings used for the residual-based approximation. All experiments use the same architecture and optimisation strategy across the seven calibrated cities.

Table 5. Network architecture.

Parameter	Value
Input dimension	3
Output dimension	1
Hidden layers	6
Neurons per layer	64
Activation function	tanh
Trainable parameters	2.1×10^4 (approximately)

Table 6. Collocation and sampling configuration.

Quantity	Value
Interior collocation points	5×10^4
Initial-condition points	5×10^3
Boundary points at $x = x_{\min}$	5×10^3
Boundary points at $x = x_{\max}$	5×10^3
Boundary points at $y = y_{\max}$	5×10^3
Sampling strategy	Uniform random

Table 7. Loss weights.

Loss component	Weight
PDE residual	1
Initial condition	10
Dry-boundary condition	10
Neumann condition	10
Saturation boundary	10

Table 8. Optimisation settings.

Parameter	Value
Initial optimizer	Adam
Adam learning rate	10^{-3}
Adam epochs	20000
Final optimizer	L-BFGS
Maximum L-BFGS iterations	5000
Stopping criterion	Relative loss tolerance 10^{-6}
Random seed	1234

Table 9. Computational environment.

Component	Specification
Programming language	Python 3
Automatic differentiation	TensorFlow
Precision	Double precision
CPU	Multi-core x86 processor
GPU	NVIDIA CUDA-compatible device
Operating system	Linux

Conflicts of Interest: The authors declare that there are no conflicts of interest regarding the publication of this paper.

References

[1] M. Raissi, P. Perdikaris, G.E. Karniadakis, Physics-Informed Neural Networks: A Deep Learning Framework for Solving Forward and Inverse Problems Involving Nonlinear Partial Differential Equations, J. Comput. Phys. 378 (2019), 686–707. https://doi.org/10.1016/j.jcp.2018.10.045.

[2] L. Yang, X. Meng, G.E. Karniadakis, B-PINNs: Bayesian Physics-Informed Neural Networks for Forward and Inverse PDE Problems with Noisy Data, J. Comput. Phys. 425 (2021), 109913. https://doi.org/10.1016/j.jcp.2020.109913.

[3] A. Dhiman, Y. Hu, Physics Informed Neural Network for Option Pricing, arXiv:2312.06711, 2023. https://doi.org/10.48550/arXiv.2312.06711.

[4] D. Hainaut, A. Casas, Option Pricing in the Heston Model with Physics Inspired Neural Networks, Ann. Financ. 20 (2024), 353–376. https://doi.org/10.1007/s10436-024-00452-7.

[5] D. Hainaut, Valuation of Guaranteed Minimum Accumulation Benefits (GMABs) with Physics-Inspired Neural Networks, Ann. Actuar. Sci. 18 (2024), 442–473. https://doi.org/10.1017/s1748499524000095.

[6] K.M. Graczyk, K. Witkowski, Bayesian Reasoning for Physics Informed Neural Networks, arXiv:2308.13222, 2023. https://doi.org/10.48550/arXiv.2308.13222.

[7] Y. Ding, S. Chen, H. Miyake, X. Li, Physics-Informed Neural Networks with Fourier Features for Seismic Wavefield Simulation in Time-Domain Nonsmooth Complex Media, arXiv:2409.03536, 2024. https://doi.org/10.48550/arXiv.2409.03536.

[8] Y. Hou, X. Li, J. Wu, Y.-G. Wang, Enhanced BPINN Training Convergence in Solving General and Multi-scale Elliptic PDEs with Noise, arXiv:2408.09340, 2024. https://doi.org/10.48550/arXiv.2408.09340.

[9] D.d.S. Santos, T.A.E. Ferreira, Neural Network Learning of Black-Scholes Equation for Option Pricing, arXiv:2405.05780, 2024. https://doi.org/10.48550/arXiv.2405.05780.

[10] X. Wang, J. Li, J. Li, A Deep Learning Based Numerical PDE Method for Option Pricing, Comput. Econ. 62 (2023), 149–164. https://doi.org/10.1007/s10614-022-10279-x.

[11] F. Gatta, V.S. Di Cola, F. Giampaolo, F. Piccialli, S. Cuomo, Meshless Methods for American Option Pricing Through Physics-Informed Neural Networks, Eng. Anal. Bound. Elem. 151 (2023), 68–82. https://doi.org/10.1016/j.enganabound.2023.02.040.

[12] A.Q. Ibrahim, S. Götschel, D. Ruprecht, Parareal with a Physics-Informed Neural Network as Coarse Propagator, in: Euro-Par 2023: Parallel Processing, Lecture Notes in Computer Science, Springer Nature Switzerland, Cham, 2023, pp. 649–663. https://doi.org/10.1007/978-3-031-39698-4_44.

[13] Y. Bai, T. Chaolu, S. Bilige, The Application of Improved Physics-Informed Neural Network (IPINN) Method in Finance, Nonlinear Dyn. 107 (2022), 3655–3667. https://doi.org/10.1007/s11071-021-07146-z.

[14] P. Li, Pricing Weather Derivatives with Partial Differential Equations of the Ornstein–Uhlenbeck Process, Comput. Math. Appl. 75 (2018), 1044–1059. https://doi.org/10.1016/j.camwa.2017.10.030.

[15] W. Tang, S. Chang, A Semi-Lagrangian Method for the Weather Options of Mean-Reverting Brownian Motion with Jump–Diffusion, Comput. Math. Appl. 71 (2016), 1045–1058. https://doi.org/10.1016/j.camwa.2015.12.040.

[16] C. Nhangumbe, E. Sousa, Numerical Solutions of an Option Pricing Rainfall Weather Derivatives Model, Comput. Math. Appl. 153 (2024), 43–55. https://doi.org/10.1016/j.camwa.2023.11.011.

[17] C. Harris, The Valuation of Weather Derivatives Using Partial Differential Equations, MSc Dissertation, University of Reading, 2003.

[18] H. Hamisultane, Which Method for Pricing Weather Derivatives?, (2008). https://shs.hal.science/halshs-00355856v1.

[19] E. Broni-Mensah, Numerical Solutions of Weather Derivatives and Other Incomplete Market Problems, PhD Thesis, The University of Manchester, 2012.

[20] P. Li, The Valuation of Weather Derivatives Using One-Sided Crank–Nicolson Schemes, Comput. Econ. 58 (2021), 825–847. https://doi.org/10.1007/s10614-020-10052-y.

[21] S. Bansal, P. Boro, S. Natesan, Physics-Informed Neural Network for Option Pricing Weather Derivatives Model, Comput. Math. Appl. 200 (2025), 1–21. https://doi.org/10.1016/j.camwa.2025.09.001.

[22] F. Black, M. Scholes, The Pricing of Options and Corporate Liabilities, J. Polit. Econ. 81 (1973), 637–654. https://doi.org/10.1086/260062.

[23] J.S. Butler, B. Schachter, Unbiased Estimation of the Black/Scholes Formula, J. Financ. Econ. 15 (1986), 341–357. https://doi.org/10.1016/0304-405X(86)90025-5.

[24] J.D. Macbeth, L.J. Merville, An Empirical Examination of the Black-Scholes Call Option Pricing Model, J. Finance 34 (1979), 1173–1186. https://doi.org/10.2307/2327242.

[25] J.P. Villarino, A. Leitao, J.A. García Rodríguez, Boundary-Safe PINNs Extension: Application to Non-Linear Parabolic PDEs in Counterparty Credit Risk, J. Comput. Appl. Math. 425 (2023), 115041. https://doi.org/10.1016/j.cam.2022.115041.

[26] L. Zeng, Weather Derivatives and Weather Insurance: Concept, Application, and Analysis, Bull. Am. Meteorol. Soc. 81 (2000), 2075–2082. https://doi.org/10.1175/1520-0477(2000)081<2075:WDAWIC>2.3.CO;2.

[27] F.E. Benth, J. Šaltytė-Benth, Modeling and Pricing in Financial Markets for Weather Derivatives, World Scientific, 2012. https://doi.org/10.1142/8457.

[28] R. Carmona, P. Diko, Pricing Precipitation Based Derivatives, Int. J. Theor. Appl. Finance 8 (2005), 959–988. https://doi.org/10.1142/S0219024905003311.

[29] M. Hess, On the Pricing and Hedging of Precipitation Derivatives, Probab. Uncertain. Quant. Risk 9 (2024), 499–528. https://doi.org/10.3934/puqr.2024021.

[30] M. Baljon, S.K. Sharma, Rainfall Prediction Rate in Saudi Arabia Using Improved Machine Learning Techniques, Water 15 (2023), 826. https://doi.org/10.3390/w15040826.

[31] M. Almazroui, M.N. Islam, P.D. Jones, H. Athar, M.A. Rahman, Recent Climate Change in the Arabian Peninsula: Seasonal Rainfall and Temperature Climatology of Saudi Arabia for 1979–2009, Atmos. Res. 111 (2012), 29–45. https://doi.org/10.1016/j.atmosres.2012.02.013.